PHYSICS AND CHEMISTRY OF SOLID STATE
V. 26, No. 3 (2025) pp. 564-577
Section: Physics

DOI: 10.15330/pcss.26.3.564-577

Vasyl Stefanyk Carpathian National University

ФІЗИКА І ХІМІЯ ТВЕРДОГО ТІЛА
Т. 26, № 3 (2025) С. 564-577
Фізико-математичні науки

PACS: 75.75.-c, 75.30.Cr, 82.70.-y, 87.85.Rs

ISSN 1729-4428 (Print)
ISSN 2309-8589 (Online)

M. Mokliak[1], L. Kaykan[2], J. Mazurenko[2], M. Moiseienko[3], M. Kuzyshyn[3], I. Dovbnia[3], N. Ilnitsky[3], S. Yuryev[4], V. Mokliak[2,5]

Influence of Neodymium Doping on the Thermomagnetic Response and Colloidal Behavior of Copper Ferrite Nanoparticles

[1]*Department of Applied Physics and Materials Science, Vasyl Stefanyk Carpathian National University, Ivano-Frankivsk, Ukraine, mariamoklyak@gmail.com*
[2]*Laboratory for Physics of Magnetic Films, G.V. Kurdyumov Institute for Metal Physics, N.A.S. of Ukraine, Kyiv, Ukraine, alekstraza0@gmail.com, mvvmcv@gmail.com ;*
[3]*Department of Medical Informatics, Medical and Biological Physics, Ivano-Frankivsk National Medical University, Ivano-Frankivsk, Ukraine, mmoiseyenko@ifnmu.edu.ua, mkuzyshyn@ifnmu.edu.ua, Ilnytskyi_Na@ifnmu.edu.ua;*
[4]*Lviv Polytechnic National University, Lviv, Ukraine, s.o.yuryev@gmail.com*
[5]*Department of Physical and Mathematical Sciences, Ivano-Frankivsk National Technical University of Oil and Gas, Ivano-Frankivsk, Ukraine, volodymyr.mokliak@nung.edu.ua,*

In this paper, $CuNd_xFe_{2-x}O_4$ (x = 0.00 - 0.11) nanoparticles were synthesized via a sol-gel autocombustion method and systematically investigated to evaluate the impact of neodymium substitution on their structural, magnetic, and heating performance for magnetic hyperthermia applications. X-ray diffraction confirmed the formation of spinel structures across all compositions. Magnetic characterization revealed a non-monotonic trend in saturation magnetization (Ms), reaching a maximum value of 62.11 emu/g at x = 0.05, while coercivity (Hc) varied between 236 and 273 Oe, reflecting the influence of Nd^{3+} on magnetic anisotropy. The magnetocrystalline anisotropy constant (K) was evaluated using both coercivity-based and high-field approaches, confirming enhanced anisotropy at moderate Nd substitution. Corresponding Néel relaxation times (τ_N) ranged from ~5 to 22 ns, supporting efficient magnetic heating for selected compositions.

Zeta potential measurements demonstrated enhanced colloidal stability with moderate Nd substitution, with values exceeding +30 mV, suggesting favorable dispersion conditions for biomedical use. Magnetic hyperthermia performance was assessed under an alternating magnetic field (23.8 kA/m, 357 kHz) using both Box–Lucas and Newton Cooling models. The highest specific absorption rate (SAR) values, were observed for x = 0.03, 0.05, and 0.11. These findings underscore the importance of optimizing rare-earth substitution to modulate surface charge, magnetic anisotropy, and relaxation behavior.

Keywords: Copper Ferrite, Neodymium substitution, Magnetic nanoparticles, Magnetic hyperthermia, Energy-efficient therapy, Box Lucas Method, Newton Cooling Approach.

Received 29 March 2025; Accepted 28 August 2025.

Introduction

Magnetic hyperthermia is a minimally invasive therapeutic modality that has gained significant attention for its potential in cancer treatment. Approved for clinical use in Europe in 2011, magnetic hyperthermia relies on the ability of magnetic nanoparticles (MNPs) to convert energy from an alternating magnetic field (AMF) into localized heat, enabling targeted thermal ablation of tumor tissues while minimizing systemic side effects [1–4]. This localized heating can also enhance the efficacy of other therapeutic approaches such as chemotherapy and radiotherapy.

The heating performance of MNPs is quantitatively described by the specific absorption rate (SAR) and intrinsic loss power (ILP), which depend on both extrinsic (field strength and frequency) and intrinsic (material-

specific) parameters [5, 6]. Among the latter, magnetic saturation (Ms), coercivity (Hc), anisotropy constant (K), and superparamagnetic behavior critically influence the energy dissipation mechanisms – namely Néel and Brownian relaxations [7-9]. Efficient heat generation requires a delicate balance between these properties, tailored to the AMF conditions and biological environment.

Recent studies emphasize that structural features such as particle size, crystallinity, and magnetic anisotropy directly affect the magnetothermal response [10, 11]. Equally important is the colloidal stability of nanoparticle dispersions, which rules their biodistribution, retention, and in vivo heating uniformity. Zeta potential, a key indicator of colloidal stability, is widely used to assess the electrostatic interactions that prevent aggregation and maintain dispersibility [12, 13]. Aggregation alters the hydrodynamic size and relaxation dynamics of MNPs, often reducing SAR due to suppressed Brownian motion and uneven heating profiles [14].

Despite substantial progress, a comprehensive understanding of how intrinsic magnetic properties and colloidal behavior jointly influence heating efficiency remains limited – especially for spinel ferrites incorporating rare-earth elements. Among these, copper ferrite ($CuFe_2O_4$) is a promising candidate due to its moderate magnetization, chemical tunability, and biocompatibility. Incorporation of trivalent neodymium (Nd^{3+}) can induce modifications in cation distribution, crystal symmetry, and surface charge, thereby affecting both the magnetic and colloidal characteristics of the system.

In this study, we investigate a series of neodymium-substituted copper ferrite ($CuNd_xFe_{2-x}O_4$) nanoparticles synthesized via a sol-gel autocombustion method. We focus on establishing direct correlations between magnetic parameters (Ms, Hc, anisotropy) derived from vibrating sample magnetometry (VSM), colloidal stability (zeta potential), and heating efficiency (SAR, ILP) under AMF exposure. By systematically varying Nd content, we aim to elucidate the structure-property-performance relationships leading magnetothermal behavior.

I. Materials and Methods

1.1. Synthesis of Nd-Substituted Copper Ferrite Nanoparticles

Neodymium-substituted copper ferrite nanoparticles ($CuNd_xFe_{2-x}O_4$, where x = 0.00-0.11) were synthesized via the sol-gel autocombustion technique [15]. Analytical grade precursors such as iron (III) nitrate nonahydrate ($Fe(NO_3)_3{\cdot}9H_2O$), copper (II) nitrate trihydrate ($Cu(NO_3)_2{\cdot}3H_2O$), neodymium (III) nitrate hexahydrate ($Nd(NO_3)_3{\cdot}6H_2O$), and citric acid monohydrate ($C_6H_8O_7{\cdot}H_2O$) were used as received without further purification. Metal nitrates were taken in stoichiometric ratios and dissolved in distilled water, then citric acid solution was added, serving as both complexing agent and fuel. The blend was mixed under constant stirring, and the pH was adjusted to ~7 using 25% aqueous ammonia solution [16]. The resulting sol was heated at ~80 °C to form a viscous gel, which upon further heating at 250–300 °C underwent a self-propagating combustion reaction, yielding a voluminous and porous ferrite powder. The as-synthesized (unannealed) sample was labeled F0, while Nd-substituted compositions were denoted as N1 to N11 corresponding to x = 0.01, 0.03, 0.05, 0.07, 0.09, and 0.11.

1.2. Structural and Microstructural Characterization

Phase identification and structural analysis were performed using an Empyrean PANalytical powder X-ray diffractometer (Malvern Panalytical, UK) operating in Bragg–Brentano geometry with Cu Kα radiation (λ = 1.5406 Å). Diffraction patterns were recorded in the 2θ range of 20°–90°, with a step size of 0.033° and scan duration of 25 minutes following a 20-minute stabilization of the sample stage to minimize thermal drift.

Transmission electron microscopy (TEM) was carried out using a FEI Tecnai G2 20 instrument (FEI, USA) equipped with a LaB_6 filament and operated at 200 kV. Powdered samples were ultrasonically dispersed in ethanol, and a drop of the suspension was deposited on carbon-coated copper grids for imaging.

1.3. Zeta Potential Measurement

Zeta potential was determined using electrophoretic light scattering (ELS) on a Zetasizer Ultra analyzer (Malvern Instruments, UK). For each measurement, 0.1 mg/mL dispersions were prepared by suspending the nanopowders in deionized water, followed by 60-minute sonication to ensure uniform dispersion. The pH of all suspensions was maintained at ~5.5. Measurements were conducted at 25 °C using folded capillary cells, and each sample was measured in triplicate to ensure reproducibility.

1.4. Magnetic Property Measurement

Magnetic hysteresis loops were recorded at room temperature using a LakeShore Model 7407 vibrating sample magnetometer (VSM, USA). Measurements were performed under a maximum applied magnetic field of ±5 kOe to extract key parameters such as saturation magnetization (Ms), coercivity (Hc), and remanence (Mr).

1.5. Magnetic Hyperthermia Evaluation

The heating efficiency of the nanoparticles under an alternating magnetic field (AMF) was assessed using a dedicated hyperthermia setup. Approximately 0.4 mL of aqueous nanoparticle dispersion was loaded into a polymeric Eppendorf tube and placed within the center of a water-cooled induction coil (2.5 cm diameter). A fiber-optic temperature probe was immersed directly into the sample to record real-time temperature evolution. AMF was generated using an EASY Heat 0224 system (Ambrell, USA), operating at a frequency of 305 kHz. Magnetic field amplitudes were varied between 23.8 and 35.7 kA/m by adjusting generator power from 0.6 to 1.6 kW. For specific absorption rate (SAR) determination, a field strength of 23.8 kA/m was used consistently across all samples. SAR values were calculated from the initial slope of the temperature-time curve, normalized by the nanoparticle concentration.

II. 2. Results and discussion

2.1. Structural Studies

Figure 1(a) displays the X-ray diffraction (XRD) patterns of the synthesized $CuNd_xFe_{2-x}O_4$ nanoparticle series. All compositions exhibit well-defined diffraction peaks that can be indexed to a cubic spinel structure with space group Fd3m.

The average crystallite size was calculated from the broadening of the most intense diffraction peaks using the Scherrer formula [17]. Across the investigated compositions, crystallite sizes were found to range from approximately 17 to 22 nm. These values are consistent with the grain dimensions observed in the transmission electron microscopy (TEM) images shown in Figure 1(b). The TEM micrographs further confirm the nanocrystalline nature of the powders.

Incorporation of Nd^{3+} ions into the spinel lattice predominantly occurs at octahedral (B) sites due to their larger ionic radius (0.983 Å) compared to Fe^{3+} (0.645 Å) [18, 19]. This substitution introduces localized lattice distortion and strain, which expand the unit cell and alter cation distribution. Such distortions influence superexchange interactions between Fe^{3+} ions at tetrahedral and octahedral sites, thereby modulating the net magnetic moment and anisotropy of the system.

From the perspective of magnetic hyperthermia, moderate Nd substitution enhances magnetocrystalline anisotropy and promotes efficient energy dissipation via Néel relaxation. However, excessive incorporation may lead to structural disorder, weakened magnetic coupling, and reduced heating efficiency.

2.2. Magnetic Studies

The magnetic properties of the $CuNd_xFe_{2-x}O_4$ nanoparticles were systematically investigated at room temperature using a vibrating sample magnetometer (VSM). Figure 2 presents the magnetization (M) versus applied magnetic field (H) hysteresis loops.

All samples display well-defined hysteresis loops, characteristic of ferrimagnetic materials. The saturation magnetization (Ms), remanent magnetization (Mr), and

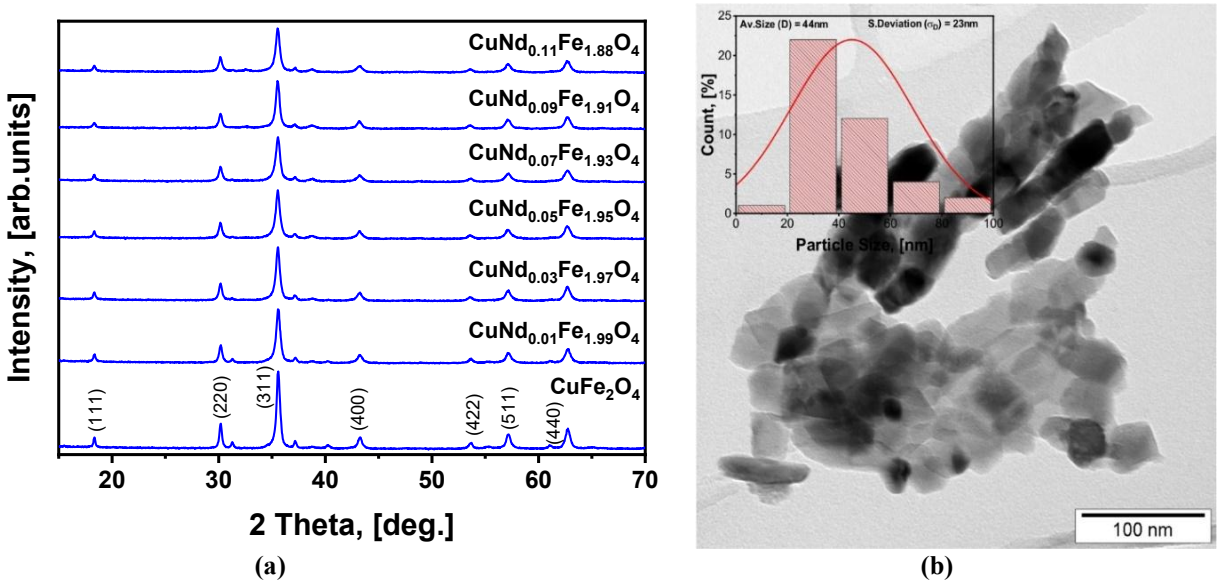

(a) (b)

Fig. 1. (a) XRD diffraction patterns of $CuNd_xFe_{2-x}O_4$ samples; (b) TEM image of $CuNd_xFe_{2-x}O_4$ sample.

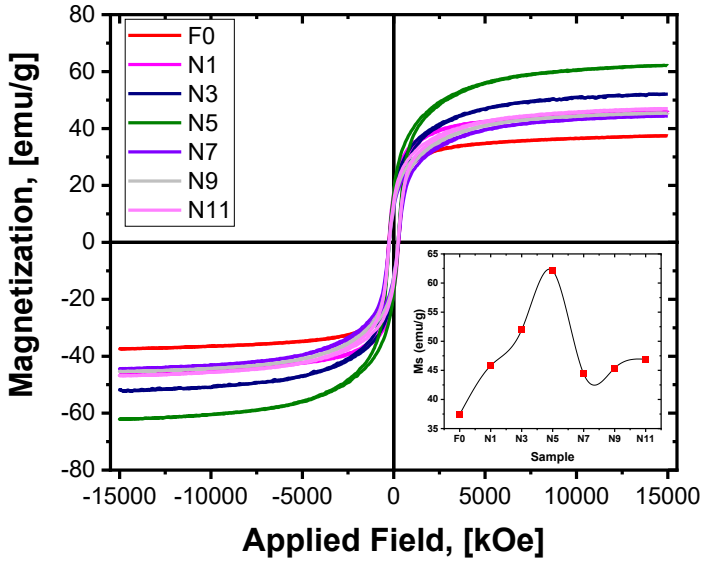

Fig. 2. Room-temperature magnetic characterization of $CuNd_xFe_{2-x}O_4$ samples.

coercivity (Hc) were extracted from the M–H curves, and the results are summarized in Table 1. The observed values of Ms ranged from 37.4 to 62.1 emu/g, with the highest magnetization recorded for the sample containing 5 at.% Nd substitution (N5). This enhancement in Ms at moderate doping levels is likely due to optimized cation redistribution between the tetrahedral (A) and octahedral (B) sites, improving superexchange interactions [20]. At higher substitution levels, a reduction in Ms may result from increased magnetic dilution or spin disorder associated with the incorporation of larger, magnetically less-coupled Nd^{3+} ions [21, 22].

To further assess magnetic behavior, the squareness ratio (Mr/Ms) and coercivity efficiency (Hc/Mr) were calculated (table 1). The squareness ratio, defined as the ratio of remanent magnetization (Mr) to saturation magnetization (Ms), ranged from 0.27 to 0.38 across the $CuNd_xFe_{2-x}O_4$ samples. Values significantly below 0.5 typically indicate the presence of multi-domain or pseudo-single-domain particles, where magnetization reversal involves domain wall motion rather than coherent rotation [23, 24].

The magnetocrystalline anisotropy constant (K) was estimated using the expression [25]:

$$K = \frac{H_c \times M_S}{0.96}$$

This model, adapted from the Stoner-Wohlfarth framework [26], assumes non-interacting, randomly oriented, single-domain particles. The calculated K values fall within the range of 0.56×10^5 to 0.87×10^5 erg/cm^3, confirming moderate anisotropy contributions that influence coercive field strength.

The effective magnetic moment per formula unit (μ_{eff}) was also estimated using [25]:

$$\mu_{eff} = \frac{M_S \times M_W}{5585}$$

where Mw is the molar mass of $CuNd_xFe_{2-x}O_4$, and 5585 is the conversion factor to μB/f.u. The calculated μ_{eff} values span from 1.60 to 2.71 μB, reflecting compositional modulation of the magnetic sublattice.

To better understand the anisotropy of the nanoparticles, the magnetization curves were analyzed in the high-field region (H > 2000 Oe) using the Law of Approach to Saturation (LAS) [26, 27]. This method works well for cubic magnetic materials, where at high magnetic fields, domain wall motion is minimal, and magnetization increases mainly through the rotation of magnetic moments.

The LAS model is expressed as [25, 27]:

$$M = M_S\left(1 - \frac{A}{H} - \frac{B}{H^2}\right) + kH$$

Here: *a/H* accounts for microstructural defects, porosity, and internal stress; b/H^2 is associated with magnetocrystalline anisotropy energy; *kH* represents the field-induced paramagnetic contribution, relevant only at very high fields or elevated temperatures.

To validate this approach, experimental M(H) curves were fitted using the above expression for all samples. The parameter *b* was used to estimate the anisotropy constant K_1 using the relation [25, 27]:

$$K_1 = \mu_0 M_S \sqrt{\frac{105b}{8}}$$

The fitting results, including extracted values of *a*, *b*, *k*, *Ms*, and corresponding coefficients of determination (R^2), are presented in Table 2. The fits, shown in Figure 3, demonstrate excellent agreement ($R^2 \approx 0.99$), indicating strength of the LAS model in describing the high-field magnetization behavior of the Nd-substituted ferrites.

Based on the fitting results, the magnetic anisotropy constant (*K*) of $CuNd_xFe_{2-x}O_4$ nanoparticles was evaluated using two methods: one derived from high-field LAS fitting, and the other from coercivity (*Hc*). Magnetic anisotropy determines how easily the magnetization direction changes, and comparing these two methods helps clarify which factors affect this property.

The coercivity-based method is based on the Stoner–Wohlfarth model and uses *Hc* and *Ms* to estimate *K*. While straightforward, this approach reflects not only the intrinsic magnetocrystalline anisotropy but also external factors such as particle shape, surface irregularities, and interactions between particles. Moreover, the model assumes ideal conditions – zero temperature, coherent rotation, and no interparticle effects – which are rarely met in real nanoparticle systems. As a result, the *K* values obtained this way often represent an effective anisotropy and may be overestimated.

In contrast, the LAS method analyzes how

Table 1.

Room-temperature magnetic parameters of $CuNd_xFe_{2-x}O_4$ samples annealed at different temperatures, obtained from VSM measurements.

Samples	Ms, [emu/g]	Mr, [emu/g]	Hc, [Oe]	M_R/M_S	K × 10^5, [egr/cm^3]	H_C/M_R	μ_{eff}, [μ_B/f.u.]
Nd0	37.42	14.13	265.92	0.38	0.56	18.82	1.60
Nd1	45.81	17.56	272.27	0.38	0.70	15.51	1.97
Nd3	51.96	15.16	243.80	0.29	0.72	16.09	2.25
Nd5	62.11	17.50	247.66	0.28	0.87	14.16	2.71
Nd7	44.40	11.83	256.70	0.27	0.65	21.71	1.95
Nd9	45.40	12.58	236.16	0.28	0.61	18.77	2.01
Nd11	46.91	14.42	243.98	0.31	0.65	16.92	2.09

M_S – saturation magnetization; M_R – remanent magnetization; H_C – coercivity; T_C – Curie temperature; M_R/M_S – squareness ratio; K – magnetic anisotropy constant; H_C/M_R – coercivity efficiency ratio; μ_{eff} – effective magnetic moment per formula unit.

magnetization approaches saturation at high magnetic fields, where irreversible processes like domain wall motion are minimized. The LAS-derived K_1 is linked to the rotation of magnetic moments against the crystal's anisotropy and is less influenced by external effects. Therefore, it is considered a more accurate estimate of intrinsic magnetocrystalline anisotropy.

As shown in Table 2, both methods reveal similar trends with neodymium substitution: K increases up to x = 0.05, then decreases. This behavior suggests that moderate Nd content enhances anisotropy – likely by introducing local structural distortion – while excessive substitution disrupts magnetic order and lowers anisotropy.

To better understand the magnetic energy dissipation mechanisms underlying hyperthermia performance, the Néel relaxation time (τ_N) [28] was estimated for all $CuNd_xFe_{2-x}O_4$ compositions. Néel relaxation describes the thermally activated reorientation of magnetic moments within single-domain nanoparticles, driven by overcoming the anisotropy energy barrier. It is the dominant mechanism in solid or viscous media where Brownian rotation is suppressed.

The Néel relaxation time (τ_N) is defined as [29]:

$$\tau_N = \tau_0 exp\left(\frac{KV}{k_B T}\right)$$

Where τ_0 is the characteristic attempt time

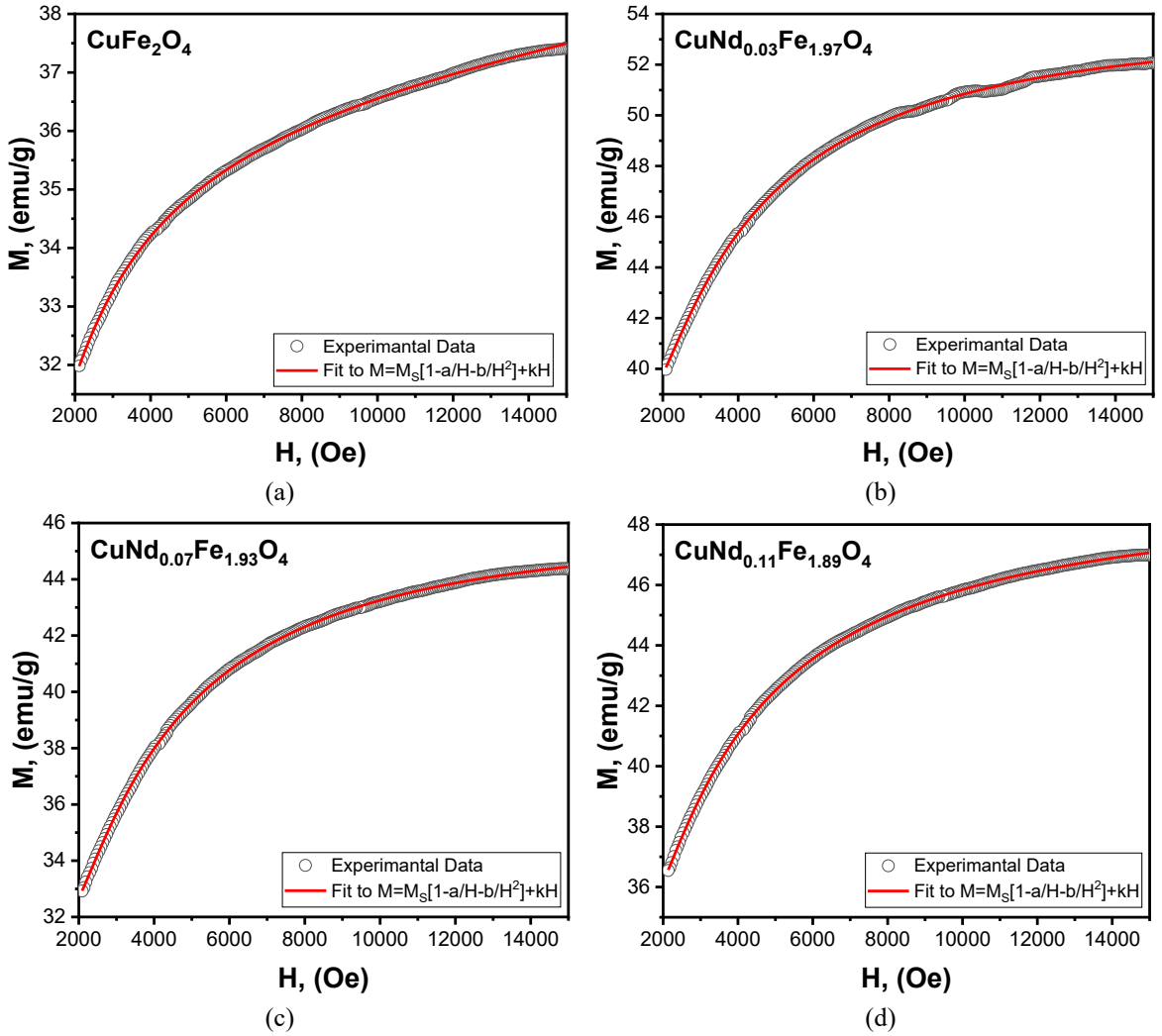

Fig. 3. High-field fitting of $CuNd_xFe_{2-x}O_4$ samples using the Law of Approach to Saturation (LAS).

Table 2

Parameters obtained from LAS fitting and calculated anisotropy constant K_1 for $CuNd_xFe_{2-x}O_4$ samples.

Sample	Ms, emu/g	a, Oe	b × 10^3, Oe^2	k × 10^{-5}, emu/g·Oe	R^2	K_1, × 10^5 [erg/cm^3]	τ_N, × 10^{-9} s
$CuFe_2O_4$	36.86	379 ± 5	-184 ± 8	10.22 ± 0.17	0.99	0.14	6.11
$CuNd_{0.01}Fe_{1.99}O_4$	45.94	484 ± 9	-311 ± 10	9.60 ± 0.39	0.99	0.20	5.23
$CuNd_{0.03}Fe_{1.97}O_4$	56.25	935 ± 7	-707 ± 12	5.44 ± 0.42	0.99	0.31	16.75
$CuNd_{0.05}Fe_{1.95}O_4$	66.95	931 ± 3	-679 ± 6	5.27 ± 0.26	0.99	0.37	14.00
$CuNd_{0.07}Fe_{1.93}O_4$	48.59	1055 ± 4	-810 ± 7	6.01 ± 0.24	0.99	0.28	6.89
$CuNd_{0.09}Fe_{1.91}O_4$	49.70	966 ± 3	-701 ± 6	8.05 ± 0.19	0.99	0.28	22.10
$CuNd_{0.11}Fe_{1.89}O_4$	49.97	868 ± 3	-632 ± 6	1.02 ±0.19	0.99	0.27	7.84

(~10^{-9} s), K is the magnetocrystalline anisotropy constant (in J/m³), V is the magnetic core volume of a nanoparticle, k_B is the Boltzmann constant (1.38×10^{-23} J/K), T is the absolute temperature (300 K).

For this analysis, the anisotropy constant K was taken from the LAS high-field fitting, as it provides a more intrinsic estimation of the magnetocrystalline contribution compared to the coercivity-based approach. The particle volume V was calculated assuming a spherical geometry and using the average crystallite size d derived from XRD analysis:

$$V = \frac{\pi}{6} d^3$$

where d is expressed in meters. The calculated values of τ_N were then compared to the characteristic period of the applied alternating magnetic field (AMF), $\tau_{AMF}=1/f$, with f = 357 kHz (i.e., $\tau_{AMF}\approx 2.8$ μs).

If $\tau_N \ll \tau_{AMF}$, the particle magnetization can follow the field oscillations effectively, leading to high SAR values via Néel relaxation. Conversely, larger τ_N values indicate reduced relaxation efficiency and lower heat dissipation.

As summarized in Table 2, the Néel relaxation times (τ_N) for the $CuNd_xFe_{2-x}O_4$ series span a narrow nanosecond range, from approximately 5.23×10^{-9} s to 22.10×10^{-9} s, indicating fast relaxation behavior across all compositions. This dynamic range is governed by the combined effects of magnetocrystalline anisotropy (K_1) and particle volume, both of which directly influence the thermal energy barrier (KV/k_BT) for magnetization reversal.

The relaxation time shows a non-linear dependence on Nd content, closely mirroring the evolution of the anisotropy constant. For example, the x = 0.09 sample exhibits the longest τ_N (22.10 ns) due to its relatively large particle size (20.6 nm) combined with moderate anisotropy ($K_1 = 0.28 \times 10^5$ erg/cm³). Conversely, samples with lower K_1 and/or smaller diameters – such as $CuFe_2O_4$ (x = 0) and x = 0.01 – exhibit shorter τ_N values (6.11 ns and 5.23 ns, respectively), indicative of more rapid magnetic moment fluctuations.

Interestingly, the x = 0.03 and 0.11 samples display intermediate τ_N values (16.75 and 7.84 ns, respectively), suggesting a favorable balance between anisotropy and size for efficient energy dissipation. These values fall within the optimal relaxation window for magnetic hyperthermia under an alternating magnetic field (AMF) of 23.8 kA/m and 357 kHz, where τ_N is expected to be comparable to the AMF period ($1/f \approx 2.8$ μs). While none of the samples reach the microsecond regime, the τ_N/τ_{AMF} ratio remains sufficiently low to permit effective Néel-based heating in the clinical frequency range.

The x = 0.05 composition, with high anisotropy ($K_1 = 0.37 \times 10^5$ erg/cm³) and moderate τ_N (14.00 ns), aligns well with its superior SAR performance, confirming the relevance of finely tuned magnetic anisotropy in maximizing hyperthermia output. These results suggest that moderate Nd substitution enables precise control over the Néel relaxation regime, providing a strategy to engineer spinel ferrite nanoparticles with optimized thermal response for biomedical applications.

2.3. Zeta potential measurements

Colloidal stability is a key factor affecting the performance and biocompatibility of magnetic nanoparticles (MNPs), especially in magnetic hyperthermia (MH) [30]. Zeta potential reflects the electrostatic potential at the slipping plane between a particle's surface and the surrounding fluid [12, 31]. It is widely used to evaluate the stability of colloidal dispersions. High absolute values of zeta potential (positive or negative) indicate strong repulsion between particles, reducing aggregation and improving dispersion stability. Values close to zero, by contrast, suggest poor stability and a tendency for particles to agglomerate.

In the context of MH, stable dispersions help ensure uniform heat generation, reduce localized overheating, and support consistent temperature control during treatment. Moreover, in biological systems, well-dispersed nanoparticles exhibit prolonged circulation time and reduced clearance by the reticuloendothelial system (RES). Aggregation not only affects biodistribution but also impacts heating efficiency by altering the effective hydrodynamic diameter and diminishing the contribution from Brownian relaxation, potentially lowering the specific absorption rate (SAR).

Zeta potential was measured using electrophoretic light scattering [32]. Nanoparticle suspensions were introduced into a folded capillary cell, and an external electric field was applied. Charged particles moved toward the oppositely charged electrode with a velocity proportional to their electrophoretic mobility (μ_e), which was determined from the Doppler shift of scattered laser light.

The zeta potential (ζ) was then calculated using the Smoluchowski approximation [33]:

$$\zeta = \frac{\mu_e \times \eta}{\varepsilon}$$

Where ζ is the zeta potential (in Volts, V); μ_e is the electrophoretic mobility (in $m^2V^{-1}s^{-1}$); η is the dynamic viscosity of the dispersion medium (Pa·s); ε is the dielectric permittivity of the dispersion medium (F/m), given by $\varepsilon = \varepsilon_0 \cdot \varepsilon_r$.

Here, ε_0 is the vacuum permittivity (8.854×10^{-12} F/m), and ε_r is the relative dielectric constant of water (≈ 78.5 at 25 °C).

The zeta potential measurements of the $CuNd_xFe_{2-x}O_4$ nanoparticles revealed a non-linear dependence on neodymium content, highlighting the sensitivity of surface charge behavior to compositional modification. The undoped $CuFe_2O_4$ sample exhibited a modest positive zeta potential of +12.40 mV, indicating limited electrostatic repulsion and a moderate tendency toward aggregation in aqueous dispersions. Upon initial Nd^{3+} substitution (x = 0.01–0.05), the zeta potential increased significantly, reaching a maximum of +32.24 mV at x = 0.05. This enhancement is attributed to neodymium-induced changes in surface chemistry, such as altered protonation–deprotonation behavior of surface hydroxyl groups, modification of the electrical double layer, and shifts in surface complexation equilibria. The larger ionic radius and trivalent charge of Nd^{3+} also influence local coordination environments and stabilize a more uniform

surface structure, leading to increased surface charge and colloidal stability. These effects are particularly beneficial for magnetic hyperthermia applications, where well-dispersed nanoparticles minimize aggregation-induced dipolar interactions and enable efficient Brownian and Néel relaxation heating pathways.

At higher substitution levels ($x \geq 0.07$), the zeta potential declined markedly, with a drop to +20.68 mV for $x = 0.11$, suggesting that excessive Nd^{3+} incorporation introduces surface disorder, lattice strain, or saturation of charge-compensating sites. Additionally, Nd-rich domains or partial surface segregation could alter hydration shells and reduce electrostatic repulsion through charge screening and surface reconstruction. These changes compromise colloidal stability, increase the likelihood of particle agglomeration, and adversely affect heating homogeneity and therapeutic performance.

From a biomedical standpoint, particles with zeta potential magnitudes above +30 mV are generally

less likely to be recognized and tagged by immune proteins for removal (a process known as opsonization, where particles are marked for clearance by immune cells). Rapid clearance by the mononuclear phagocyte

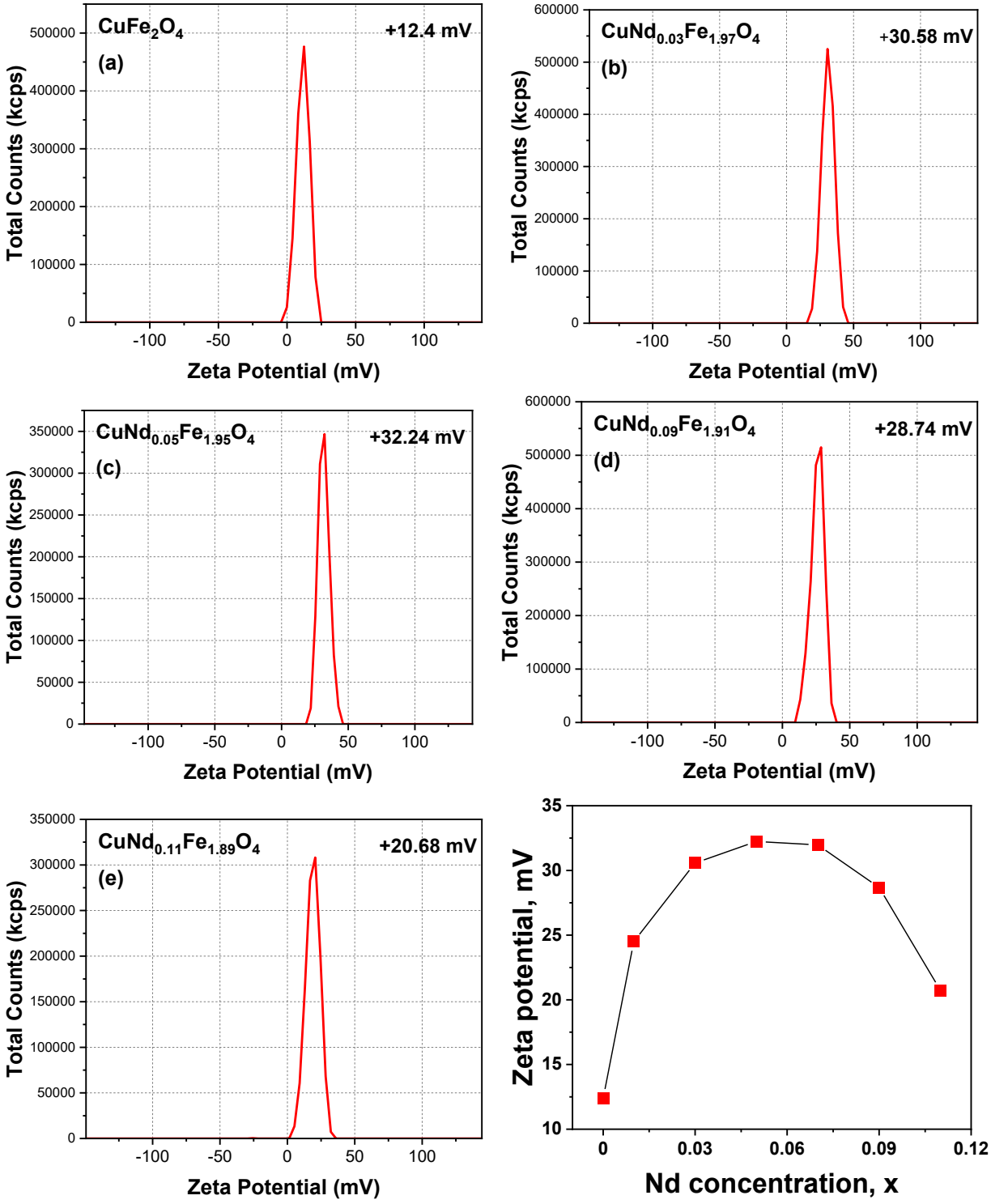

Fig. 4. Zeta potential of $CuNd_xFe_{2-x}O_4$ samples.

system, improving blood circulation time and enhancing tumor accumulation via the enhanced permeability and retention (EPR) effect. Furthermore, since zeta potential tends to be reduced in physiological media due to ionic screening, a high initial surface charge provides a necessary buffer to maintain dispersion stability under biologically relevant conditions.

2.3. Inductive Heating Behavior

The inductive heating behavior of $CuNd_xFe_{2-x}O_4$ nanoparticles was evaluated by applying an alternating magnetic field (AMF) with an amplitude of 23.8 kA/m and a frequency of 357 kHz [34]. As shown in Figure 6, the time-dependent temperature profiles for samples with varying neodymium content (x = 0.00–0.11) reveal differences in heating rates and saturation temperatures, highlighting the influence of compositional and thermal treatment on magnetic energy conversion efficiency.

To mimic biologically relevant conditions, the nanoparticles were embedded in a 2 wt% agar matrix, which replicates the porosity, viscosity, and thermal conductivity of soft tissue. The sample preparation followed a modified protocol based on Serantes et al. [35], involving two stages of sonication to ensure homogeneous dispersion: the first at 70 °C for 10 minutes to liquefy the agar and disperse the particles, followed by a second 60-minute step after agar addition. The final suspensions (1 mg/mL nanoparticle concentration) were loaded into custom-designed holder with constant volume and geometry to eliminate variability in field exposure or heat loss, as shown schematically in Figure 5.

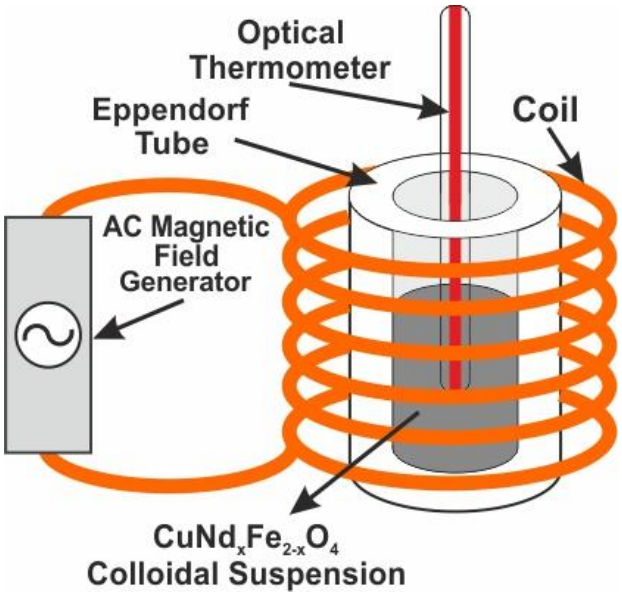

Fig. 5. Schematic representation of the experimental setup used for magnetic induction heating measurements.

The heating profiles (Figure 6) show that Nd substitution and thermal annealing significantly modulate the heating response. The inductive heating performance of $CuNd_xFe_{2-x}O_4$ nanoparticles exhibited a non-monotonic dependence on neodymium content. As depicted in Figure 6, the x = 0.05 composition (N5) demonstrated the most pronounced thermal response under AMF excitation, reaching the highest temperature increase within the measured interval. This was followed by N3 (x = 0.03) and N11 (x = 0.11), while the undoped $CuFe_2O_4$ sample (F0) exhibited the weakest heating profile. The observed trend in heating efficiency –

N5 > N3 > N11 > N1 > N9 > N7 > F0 - reflects the complex relationship between intrinsic magnetic parameters (e.g., saturation magnetization, coercivity), surface charge characteristics (zeta potential), and nanoparticle dispersion quality within the agar matrix. Samples exhibiting a favorable combination of high magnetic moment and strong colloidal stability showed enhanced energy dissipation under AMF, resulting in elevated Specific Absorption Rate (SAR) values.

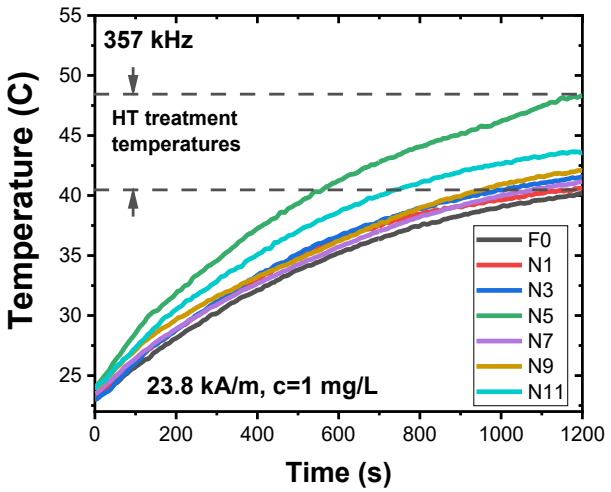

Fig. 6. Time-dependent heating curves of $CuNd_xFe_{2-x}O_4$ nanoparticles (x = 0.00–0.11) measured under an alternating magnetic field of 23.8 kA/m and 357 kHz.

2.3.1. Box Lucas Method for SAR Determination

The heating dynamics of the $CuNd_xFe_{2-x}O_4$ nanoparticle suspensions under alternating magnetic field (AMF) were quantitatively analyzed using the Box–Lucas fitting method [34, 36], which is well-suited for non-adiabatic systems where heat exchange with the environment cannot be neglected. This approach incorporates Newtonian cooling behavior and is particularly effective in modeling the typical exponential rise and subsequent thermal saturation observed in magnetic hyperthermia measurements.

Following an initial thermal equilibration phase, the time-dependent temperature evolution was fitted using the Box–Lucas equation [37]:

$$T(t) = a[1 - \exp(-b(t - t_0))]$$

where t_0=20s represents the initial time offset, and *a* and *b* are fitting constants. The parameter a corresponds to the maximum temperature increase, while b reflects the effective heating rate.

The Specific Absorption Rate (SAR), which quantifies the heat dissipated per unit mass of magnetic material, was calculated from the Box–Lucas parameters using [37]:

$$SAR_{Box-Lucas} = \frac{M_S}{M_n} \times C(a \times b)$$

where C is the specific heat capacity of the medium

(4.13 J·g⁻¹·°C⁻¹ for 2 wt% agar); Ms = 1.5 g is the total mass of the suspension; Mn = 0.01 g is the mass of magnetic nanoparticles.

To assess the intrinsic heating efficiency of the materials independently of applied field conditions, the Intrinsic Loss Power (ILP) was calculated as [34, 38]:

$$ILP = \frac{SAR}{H^2 f}$$

where H = 23.8 kA/m is the field amplitude and f = 357 kHz is the excitation frequency.

Representative Box–Lucas fits of the experimental heating curves are shown in Figure 7, demonstrating good agreement between the model and the measured temperature profiles. The corresponding SAR and ILP values derived from the fits are summarized in Table 3. A clear non-monotonic trend in heating efficiency is observed across the $CuNd_xFe_{2-x}O_4$ series. The sample with x = 0.05 ($CuNd_{0.05}Fe_{1.95}O_4$) exhibited the highest SAR of 33.03 W/g and ILP of 0.163 nH·m²/kg, indicating optimal energy conversion under AMF. Interestingly, a comparable SAR of 33.43 W/g and ILP of 0.165 nH·m²/kg was also recorded for x = 0.11, despite its lower zeta potential and saturation magnetization, suggesting the

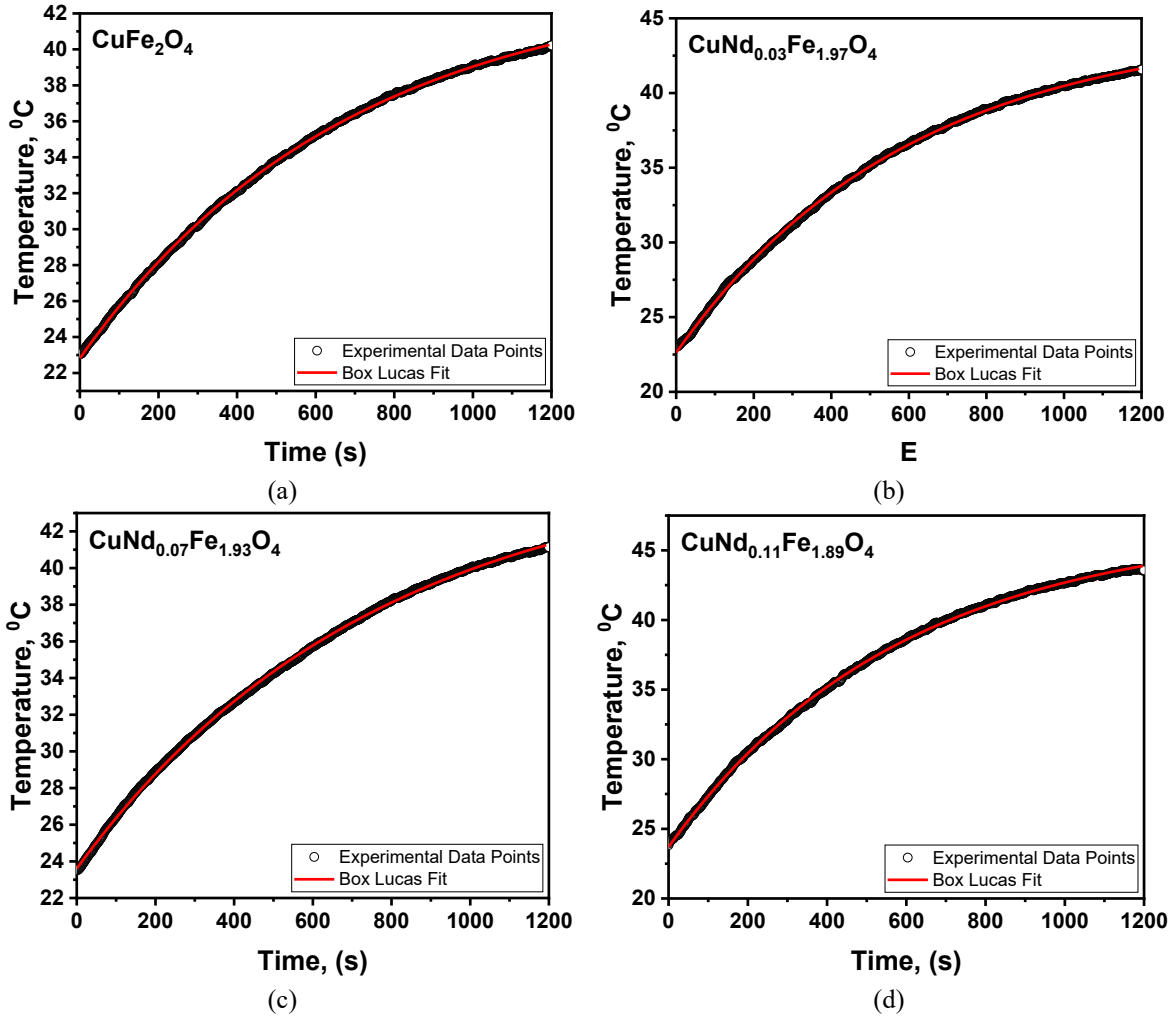

Fig. 7. Box–Lucas fitting of time-dependent heating curves for $CuNd_xFe_{2-x}O_4$ nanoparticles under 23.8 kA/m and 357 kHz AMF.

Table 3.

SAR and ILP values of $CuNd_xFe_{2-x}O_4$ nanoparticles calculated from Box–Lucas and Newton Cooling fits. Magnetic properties (*Ms*, *Hc*) are shown for correlation.

	Box-Lucas Fit		Newton Cooling Approach Fit			
Sample	**SAR, W/g**	**ILP, nH·m²/kg**	**SAR, W/g**	**ILP, nH·m²/kg**	**Ms, emu/g**	**Hc, Oe**
$CuFe_2O_4$	26.79	0.133	20.90	0.103	37.42	265.92
$CuNd_{0.01}Fe_{1.99}O_4$	31.79	0.157	25.23	0.125	45.81	272.27
$CuNd_{0.03}Fe_{1.97}O_4$	31.08	0.154	23.67	0.117	51.96	243.80
$CuNd_{0.05}Fe_{1.95}O_4$	33.03	0.163	26.54	0.131	62.11	247.66
$CuNd_{0.07}Fe_{1.93}O_4$	25.13	0.124	19.41	0.096	44.40	256.70
$CuNd_{0.09}Fe_{1.91}O_4$	23.40	0.116	17.86	0.088	45.40	236.16
$CuNd_{0.11}Fe_{1.89}O_4$	33.43	0.165	25.36	0.125	46.91	243.98

possible contribution of enhanced Néel relaxation or favorable anisotropy. In contrast, intermediate substitution levels (x = 0.07 and 0.09) showed reduced heating efficiency, likely due to suboptimal magnetic and colloidal characteristics.

2.3.2. Newton Cooling Approach Method

The temperature evolution of $CuNd_xFe_{2-x}O_4$ nanoparticle suspensions under an alternating magnetic field was also analyzed using the Newton Cooling Approach, which accounts for heat dissipation to the environment under non-adiabatic conditions. According to Newton's law of cooling, the time-dependent temperature increase can be expressed as [39]:

$$T = T_0 + \Delta T_{max}\left[1 - exp\left(\frac{-t}{\tau}\right)\right]$$

where T_0 is the initial temperature, ΔT_{max} is the maximum temperature increase, and τ is the characteristic thermal time constant. This model effectively captures both the heating phase and thermal equilibrium behavior of the system. The experimental temperature-time curves were fitted using this expression, and representative fits are shown in Figure 8.

Based on the fitting parameters ΔT_{max} and τ, the specific absorption rate (SAR) was calculated using the following relation [34, 39]:

$$SAR = \frac{C\Delta T_{max}}{\tau}\left(\frac{m_{sample}+m_{media}}{m_{sample}}\right)$$

where C is the specific heat capacity of the medium (4.13 J g^{-1} $°C^{-1}$ for 2 wt% agar), m_{sample} is the mass of magnetic material (0.01 g), and m_{medium} is the mass of the surrounding matrix (1.49 g).

The SAR values calculated using the Newton Cooling Approach are summarized in Table 3 and consistently show lower values compared to those obtained via the Box–Lucas fitting method. For all $CuNd_xFe_{2-x}O_4$ compositions, the Newton model yielded SAR values approximately 20–25% lower - for instance, $CuFe_2O_4$ exhibited a SAR of 20.90 W/g via Newton fitting, versus 26.79 W/g using the Box–Lucas model. The most prominent example is the x = 0.11 sample, where SAR dropped from 33.43 W/g (Box–Lucas) to 25.36 W/g (Newton). This discrepancy originates from fundamental methodological differences: the Newton approach emphasizes the initial heating slope and assumes negligible heat loss during early heating, whereas the Box–Lucas model accounts for the full heating curve, including plateau formation. In realistic, non-adiabatic conditions, continuous thermal dissipation occurs, and thus the Newton method may underestimate total energy conversion. As such, while the Newton Cooling Approach

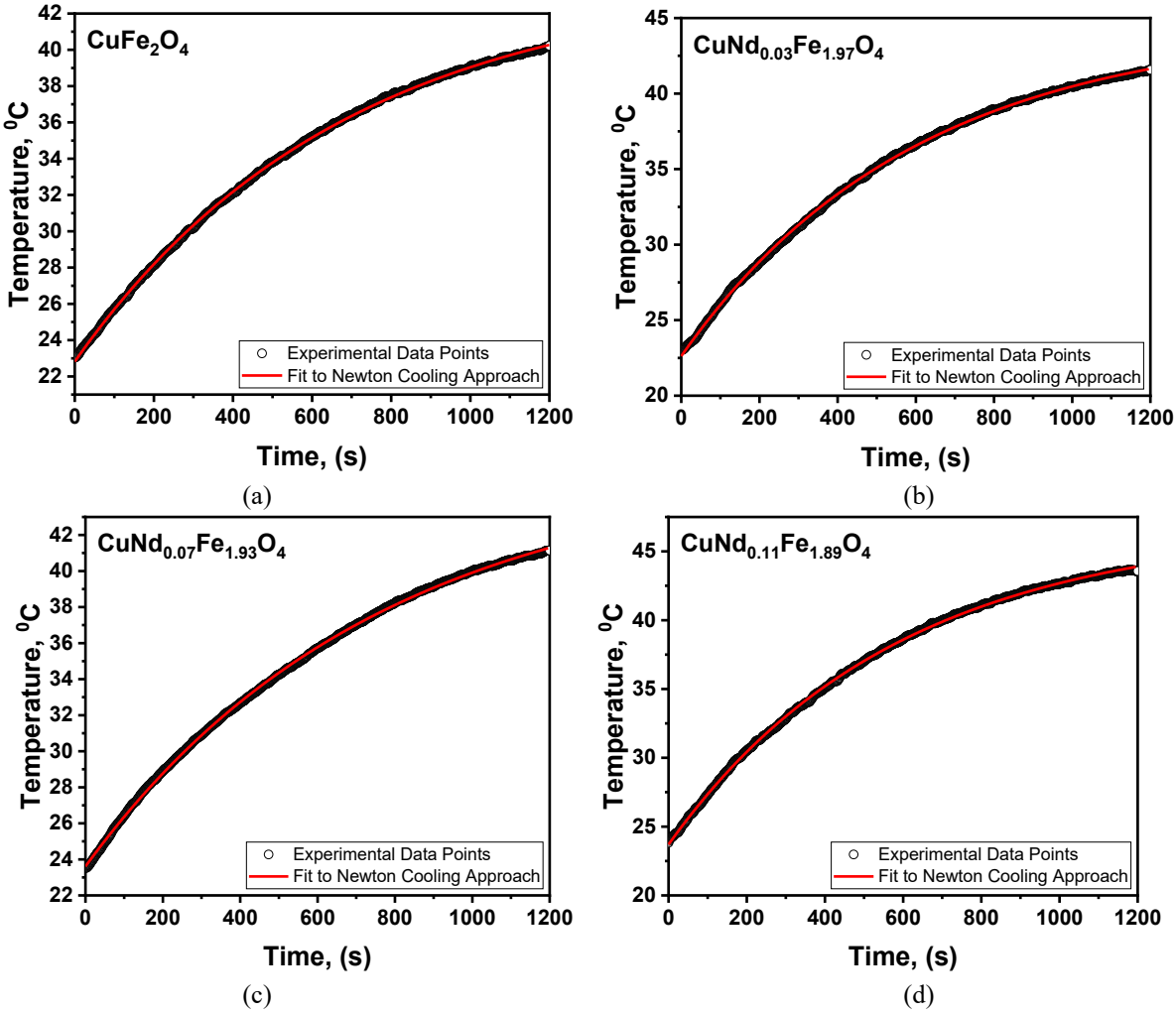

Fig. 8. Fit to the Newton Cooling Approach of time-dependent heating curves for $CuNd_xFe_{2-x}O_4$ nanoparticles under 23.8 kA/m and 357 kHz AMF.

provides a more conservative estimate, it serves as a valuable comparative tool for evaluating heating efficiency under practical constraints.

Despite using different models, the Box–Lucas and Newton Cooling methods showed consistent SAR trends across the $CuNd_xFe_{2-x}O_4$ series. The highest SAR values (31.08–33.43 W/g) were observed for x = 0.03, 0.05, and 0.11, with ILP values above 0.154 nH·m^2/kg, indicating strong heating ability under the applied AMF (23.8 kA/m, 357 kHz).

Saturation magnetization (Ms) strongly affects SAR, as it determines how much magnetic moment interacts with the field. The sample with x = 0.05 had the highest Ms (62.11 emu/g) and one of the top SAR values (33.03 W/g), confirming this link. However, the relationship is not linear: the x = 0.11 sample showed SAR (33.43 W/g) despite lower Ms (46.91 emu/g), suggesting that other factors like anisotropy and relaxation also play a role.

Zeta potential analysis showed that samples with x = 0.03–0.05 had good colloidal stability (>+30 mV), reducing aggregation and promoting Brownian relaxation in solution, which improves SAR. In contrast, x = 0.11 had lower stability (+20.68 mV) but still gave high SAR, pointing to Néel relaxation – dominant in smaller, anisotropic particles – as the key mechanism. Moderate Ms and coercivity (Hc = 243.98 Oe) likely helped efficient heat generation without major losses.

Samples with x = 0.07 and 0.09 had lower SARs (25.13 and 23.40 W/g), even with reasonable Ms (~44–45 emu/g). This may be due to too much Nd^{3+} disrupting magnetic order or increasing spin disorder, which reduces heating efficiency.

The inductive heating behavior of $CuNd_xFe_{2-x}O_4$ nanoparticles results from the combined effects of magnetization, coercivity, surface charge, and the balance between Néel and Brownian relaxation. The best performance at x = 0.05 highlights the importance of optimizing composition to achieve effective heating in biomedical applications.

Conclusions

In this study, a series of $CuNd_xFe_{2-x}O_4$ (x = 0.00–0.11) nanoparticles were successfully synthesized via a sol-gel autocombustion route and systematically evaluated for their structural, magnetic, colloidal, and magnetic hyperthermia properties. X-ray diffraction confirmed the formation of a spinel structure across all compositions, while magnetic measurements revealed enhanced saturation magnetization (up to 62.11 emu/g) and moderate coercivity values (236–273 Oe), suggesting the introduction of neodymium ions modulates magnetic anisotropy without destabilizing the ferrite lattice. Zeta potential analysis demonstrated improved colloidal stability with moderate Nd^{3+} substitution (x = 0.03–0.07), with values exceeding +30 mV, which is favorable for dispersion and biomedical applicability. A non-linear dependence of magnetic heating performance on Nd content was observed.

The magnetocrystalline anisotropy constant (K) was estimated using two methods. The Stoner–Wohlfarth approach, based on coercivity and Ms, yielded effective K values of $0.56–0.87 \times 10^5$ erg/cm^3, while the Law of Approach to Saturation (LAS) provided intrinsic values up to 0.37×10^5 erg/cm^3 for x = 0.05. The coercivity-based method reflects both intrinsic and extrinsic effects, whereas LAS isolates true magnetocrystalline anisotropy. Both approaches showed that anisotropy increases with Nd content up to x = 0.05, then decreases, suggesting enhanced local distortion at moderate doping and disorder at higher levels. The effective magnetic moment (μ_{eff}) ranged from 1.60 to 2.71 μ_B/f.u., with a maximum at x = 0.05, consistent with enhanced energy dissipation via Néel relaxation and optimal magnetic heating efficiency. To quantify this behavior, the Néel relaxation time (τ_N) was calculated using the LAS-derived K values and particle sizes. The results revealed a non-linear trend, with τ_N ranging from 5.23×10^{-9} to 22.10×10^{-9} s. The longest relaxation time was observed for x = 0.09, while moderate τ_N values for x = 0.05 and 0.11 align with their high SAR values, confirming that finely tuned anisotropy and volume favor efficient magnetic moment reversal and energy dissipation under an alternating magnetic field.

Specific Absorption Rate (SAR) and Intrinsic Loss Power (ILP), determined using both the Box–Lucas and Newton Cooling models, revealed that samples with x = 0.03, 0.05, and 0.11 delivered the highest heating efficiencies, reaching SAR values above 33 W/g and ILP values ≥ 0.154 nH·m²/kg under clinically relevant alternating magnetic field conditions (23.8 kA/m, 357 kHz).

The sample with x = 0.05 demonstrated an optimal combination of high magnetization, favorable coercivity, and colloidal stability, resulting in the most efficient magnetic heating behavior. Conversely, samples with higher Nd content (x = 0.07–0.09) exhibited reduced SAR despite reasonable magnetic properties, likely due to spin disorder and reduced relaxation efficiency. The performance of the x = 0.11 sample, despite lower zeta potential and moderate magnetization, suggests a shift toward Néel-dominated relaxation supported by favorable anisotropy.

Funding: *This work was supported by the National Academy of Sciences of Ukraine under project number 0122U002129.*

Data Availability Statement: *Data is contained within the article.*

Acknowledgments: *Author are grateful to the Department of Magnetism Institute of Experimental Physics SAS, Kosice, Slovakia for magnetic heating measurements. The authors are grateful to the Academic Centre for Materials and Nanotechnology AGH University of Krakow, Krakow, Poland for VSM measurements. Authors are grateful to the Department of Solid State Physics, AGH University of Krakow, Krakow, Poland for XRD measurements. The authors gratefully acknowledge the support and inspiration provided by the II European Chemistry School for Ukrainians (https://acmin.agh.edu.pl/en/detail/s/ii-european-chemistry-school-for-ukrainians), which contributed to the development of the research ideas presented in this work.*

Mokliak Mariia – PhD Student;
Kaykan Larysa – Doctor of Physical and Mathematical Sciences, Senior Researcher;
Mazurenko Julia – Candidate of Physical and Mathematical Sciences (Ph.D.), Research Fellow;
Moiseienko Mykola – Doctor of Biological Sciences, Professor;
Kuzyshyn Myroslav – Candidate of Physical and Mathematical Sciences (Ph.D.), Associate Professor;
Dovbnia Iryna – medical student, Medical Faculty;
Ilnitsky Nazar – medical student, Medical Faculty;
Yuryev Sergey – Candidate of Physical and Mathematical Sciences (Ph.D.), Associate Professor;
Mokliak Volodymyr – Doctor of Physical and Mathematical Sciences, Professor.

[1] W. Jiao, L. Dai, B. Yan, Y. Lyu, H. Fan, X. Liu, *Heating up the immune battle: Magnetic hyperthermia against cance,* Fundamental Research, (2024); https://doi.org/10.1016/j.fmre.2024.08.006.
[2] A. Chauhan, A. Saini, D. Sharma, *The evolution of integrated magnetic hyperthermia and chemodynamic therapy for combating cancer: a comprehensive viewpoint,* Nanoscale Advances, (2025); https://doi.org/10.1039/d4na01004c.
[3] Y. Zhang, C. Paraskeva, Q. Chen, A. Maisuradze, S. R. Ansari, T. Sarkar, V. Koliaraki, A. Teleki, *Flame-made nanoparticles for magnetic hyperthermia and MRI in colorectal cancer theranostics,* Nanoscale Advances, (2025); https://doi.org/10.1039/d5na00603a.
[4] H. Gavilán, S. K. Avugadda, T. Fernández-Cabada, N. Soni, M. Cassani, B. T. Mai, R. Chantrell, T. Pellegrino, *Magnetic nanoparticles and clusters for magnetic hyperthermia: optimizing their heat performance and developing combinatorial therapies to tackle cancer,* Chemical Society Reviews, 50(20), 11614 (2021); https://doi.org/10.1039/d1cs00427a.
[5] D. Egea-Benavente, J. G. Ovejero, M. del P. Morales, D. F. Barber, *Understanding MNPs Behaviour in Response to AMF in Biological Milieus and the Effects at the Cellular Level: Implications for a Rational Design That Drives Magnetic Hyperthermia Therapy toward Clinical Implementation,* Cancers, 13(18), 4583 (2021); https://doi.org/10.3390/cancers13184583.
[6] A. Salokhe, A. Koli, V. Jadhav, S. Mane-Gavade, A. Supale, R. Dhabbe, X.-Y. Yu, S. Sabale, , *Magneto-structural and induction heating properties of MFe_2O_4 (M = Co, Mn, Zn) MNPs for magnetic particle hyperthermia application,* SN Applied Sciences, 2(12), (2020); https://doi.org/10.1007/s42452-020-03865-x.
[7] O.M. Lemine, S. Algessair, N. Madkhali, B. Al-Najar, K. El-Boubbou, *Assessing the heat generation and self-heating mechanism of superparamagnetic Fe3O4 nanoparticles for magnetic hyperthermia application: the effects of concentration, frequency, and magnetic field,* Nanomaterials, 13(3), 453 (2023); https://doi.org/10.3390/nano13030453.
[8] Q.L. Vuong, P. Gillis, A. Roch, Y. Gossuin, , *Magnetic resonance relaxation induced by superparamagnetic particles used as contrast agents in magnetic resonance imaging: a theoretical review*, WIREs Nanomedicine and Nanobiotechnology, 9(6), (2017); https://doi.org/10.1002/wnan.1468.
[9] C.E. Botez, J. Knoop, *Non-Debye behavior of the Néel and Brown relaxation in interacting magnetic nanoparticle ensembles,* Materials, 17(16), 3957 (2024); https://doi.org/10.3390/ma17163957.
[10] Z. Ma, J. Mohapatra, K. Wei, J. P. Liu, S. Sun, *Magnetic nanoparticles: synthesis, anisotropy, and applications,* Chemical Reviews, 123(7), 3904 (2021); https://doi.org/10.1021/acs.chemrev.1c00860.
[11] J. Mazurenko, L. Kaykan, J. M. Michalik, M. Sikora, E. Szostak, O. Vyshnevskyi, K. Bandura, L. Turovska, *Enhanced synthesis of copper ferrite magnetic nanoparticles via polymer-assisted sol-gel autocombustion method for magnetic hyperthermia applications,* Journal of Nano Research, 84, 95 (2024); https://doi.org/10.4028/p-jbv1le.
[12] D.J. Pochapski, C. Carvalho dos Santos, G. W. Leite, S. H. Pulcinelli, C. V. Santilli, *Zeta potential and colloidal stability predictions for inorganic nanoparticle dispersions: effects of experimental conditions and electrokinetic models on the interpretation of results,* Langmuir, 37(45), 13379 (2021); https://doi.org/10.1021/acs.langmuir.1c02056.
[13] R.R. Retamal Marín, F. Babick, L. Hillemann, Aspects, *Zeta potential measurements for non-spherical colloidal particles – practical issues of characterisation of interfacial properties of nanoparticles,* Colloids and Surfaces A: Physicochemical and Engineering, 532, 516 (2017); https://doi.org/10.1016/j.colsurfa.2017.04.010.
[14] J. Tompkins, D. Huitink, , *Induction heating response of iron oxide nanoparticles in varyingly viscous mediums with prediction of Brownian heating contribution,* Nanoscale and Microscale Thermophysical Engineering, 24(3–4), 123 (2020); https://doi.org/10.1080/15567265.2020.1806968.
[15] J. Mazurenko, L. Kaykan, A. Zywczak, V. Kotsyubynsky, Kh. Bandura, M. Moiseienko, A. Vytvytskyi, *Study of Li-Al ferrites by nuclear magnetic resonance, UV-spectroscopy, and Mössbauer spectroscopy,* Journal of Nano- and Electronic Physics, 15(2), 02020 (2023); https://doi.org/10.21272/jnep.15(2).02020.
[16] L.S. Kaykan, J.S. Mazurenko, N.V. Ostapovych, A.K. Sijo, N.Ya. 'Ivanichok, *Effect of pH on structural morphology and magnetic properties of ordered phase of cobalt doped lithium ferrite nanoparticles synthesized by sol-gel auto-combustion method,* Journal of Nano- and Electronic Physics 12(4), 04008 (2020); https://doi.org/10.21272/jnep.12(4).04008.

[17] B.K. Ostafijchuk, V.S. Bushkova, V.V. Moklyak, R.V. lnitsky, *Synthesis and magnetic microstructure of nanoparticles of zinc-substituted magnesium ferrites,* Ukrainian Journal of Physics, 60(12), 1234 (2015); https://doi.org/10.15407/ujpe60.12.1234.

[18] İ. Şabikoğlu, L. Paralı, O. Malina, P. Novak, J. Kaslik, J. Tucek, J. Pechousek, J. Navarik, O. Schneeweiss, *The effect of neodymium substitution on the structural and magnetic properties of nickel ferrite,* Progress in Natural Science: Materials International, 25(3), 215 (2015); https://doi.org/10.1016/j.pnsc.2015.06.002.

[19] S.R. Bhongale, H.R. Ingawale, T. J. Shinde, P.N. Vasambekar, *Effect of Nd^{3+} substitution on structural and magnetic properties of Mg–Cd ferrites synthesized by microwave sintering technique* Journal of Rare Earths, 36(4), 390 (2018); https://doi.org/10.1016/j.jre.2017.11.003.

[20] V.O. Kotsyubynsky, A.B. Grubiak, V.V. Moklyak, V.M. Pylypiv, R.P. Lisovsky, *Structural, morphological, and magnetic properties of the mesoporous maghemite synthesized by a citrate method,* Metallofizika i Noveishie Tekhnologii, 36(11), 1497 (2016); https://doi.org/10.15407/mfint.36.11.1497.

[21] M.A. Almessiere, Y. Slimani, A.V. Trukhanov, A. Demir Korkmaz, S. Guner, S. Akhtar, S. E. Shirsath, A. Baykal, I. Ercan, *Effect of Nd–Y co-substitution on structural, magnetic, optical and microwave properties of NiCuZn nanospinel ferrites*, Journal of Materials Research and Technology, 9(5), 11278 (2020); https://doi.org/10.1016/j.jmrt.2020.08.027.

[22] R.A. Reddy, K.R. Rao, B. Rajesh Babu, G. K. Kumar, C. Rajesh, A. Chatterjee, N. K. Jyothi, *Structural, electrical and magnetic properties of cobalt ferrite with Nd^{3+} doping,* Rare Metals, 41(1), 240 (2019); https://doi.org/10.1007/s12598-019-01285-4.

[23] C.N. Chinnasamy, M. Senoue, B. Jeyadevan, O. Perales-Perez, K. Shinoda, K. Tohji, , *Synthesis of size-controlled cobalt ferrite particles with high coercivity and squareness ratio,* Journal of Colloid and Interface Science, 263(1), 80 (2003); https://doi.org/10.1016/s0021-9797(03)00258-3.

[24] S. Levi, R. T. Merrill, *Properties of single-domain, pseudo-single-domain, and multidomain magnetite,* Journal of Geophysical Research: Solid Earth, 83(B1), 309 (1978); https://doi.org/10.1029/jb083ib01p00309.

[25] S. Kumari, M. K. Manglam, A. Shukla, L. Kumar, P. Seal, J. P. Borah, M. Kar, *Optimization of magnetic properties and hyperthermia study on soft magnetic nickel ferrite fiber,* Physica B: Condensed Matter, 621, 413280 (2021); https://doi.org/10.1016/j.physb.2021.413280.

[26] E. Stoner, E. P. Wohlfarth, Mathematical and Physical Sciences, *A mechanism of magnetic hysteresis in heterogeneous alloys,* Philosophical Transactions of the Royal Society of London. Series A, 240(826), 599 (1948); https://doi.org/10.1098/rsta.1948.0007.

[27] M.K. Manglam, S. Kumari, L. K. Pradhan, S. Kumar, M. Kar, *Lattice strain caused magnetism and magnetocrystalline anisotropy in Zn modified barium hexaferrite,* Physica B: Condensed Matter, 588, 412200 (2020); https://doi.org/10.1016/j.physb.2020.412200.

[28] N. Zufelato, V. R. R. Aquino, N. Shrivastava, S. Mendanha, R. Miotto, A. F. Bakuzis, *Heat generation in magnetic hyperthermia by manganese ferrite-based nanoparticles arises from Néel collective magnetic relaxation,* ACS Applied Nano Materials, 5(5), 7521 (2022); https://doi.org/10.1021/acsanm.2c01536.

[29] K. Kodama, S. Hamada, K. Nashimoto, K. Aoki, K. Ohara, K. Nakazawa, Y. Ichiyanagi, *Nanoarchitectonics of PEG-coated Ni-Zn ferrite nanoparticles and mechanical analysis of heat generation by magnetic relaxation,* Journal of Inorganic and Organometallic Polymers and Materials, 32(9), 3292 (2022); https://doi.org/10.1007/s10904-022-02372-3.

[30] H. Gavilán, S. K. Avugadda, T. Fernández-Cabada, N. Soni, M. Cassani, B. T. Mai, R. Chantrell, T. Pellegrino, *Magnetic nanoparticles and clusters for magnetic hyperthermia: optimizing their heat performance and developing combinatorial therapies to tackle cancer,* Chemical Society Reviews, 50(20), 11614 (2021); https://doi.org/10.1039/d1cs00427a.

[31] Q. Zhang, R. Zhou, G. Huang, Y. Zhang, X. Sui, , *Zeta potential*, pp. Methods and Protocols in Food Science 287 (2024); https://doi.org/10.1007/978-1-0716-4272-6_22.

[32] C. N. Lunardi, A. J. Gomes, F. S. Rocha, J. De Tommaso, G. S. Patience, The Canadian Journal of Chemical Engineering, *Experimental methods in chemical engineering: zeta potential* 99(3), 627 (2021); https://doi.org/10.1002/cjce.23914.

[33] A. Serrano-Lotina, R. Portela, P. Baeza, V. Alcolea-Rodriguez, M. Villarroel, P. Ávila, *Zeta potential as a tool for functional materials development,* Catalysis Today, 423, 113862 (2023); https://doi.org/10.1016/j.cattod.2022.08.004.

[34] J. Mazurenko, L. Kaykan, V. Moklyak, M. Moklyak, M. Moiseienko, N. Ostapovych, M. Petryshyn, *Inductive heating behavior of copper ferrite magnetic nanoparticles,* Physics and Chemistry of Solid State, 26(2), 312 (2025); https://doi.org/10.15330/pcss.26.2.312-321.

[35] D. Serantes, D. Baldomir, *Nanoparticle size threshold for magnetic agglomeration and associated hyperthermia performance,* Nanomaterials,11(11), 2786 (2021); https://doi.org/10.3390/nano11112786.

[36] A. Cabral-Prieto, I. García-Sosa, E. Reguera, N. N. Entzana, H. Tadeo-Huerta, R. Ramírez-Suárez, *Estimation of the specific absorption rate in magnetic hyperthermia studies via the modified Box–Lucas and extended-CSM methods,* AIP Advances, 15(4), (2025); https://doi.org/10.1063/5.0254802.

[37] E.R.L. Siqueira, W O. Pinheiro, V.R. R. Aquino, B. C.P. Coelho, A. F. Bakuzis, R. B. Azevedo, M. H. Sousa, P. C. Morais, *Engineering gold shelled nanomagnets for pre-setting the operating temperature for magnetic hyperthermia,* Nanomaterials, 12(16), 2760 (2022); https://doi.org/10.3390/nano12162760.

[38] Y. Yan, Y. Li, J. You, K. Shen, W. Chen, L. Li, *Morphology-dependent magnetic hyperthermia characteristics of Fe_3O_4 nanoparticles,* Materials Chemistry and Physics, 329, 130045 (2025); https://doi.org/10.1016/j.matchemphys.2024.130045.

[39] N. Rmili, K. Riahi, R. M'nassri, B. Ouertani, W. Cheikhrouhou-Koubaa, E. K. Hlil, *Magnetocaloric and induction heating characteristics of $La_{0.71}Sr_{0.29}Mn_{0.95}Fe_{0.05}O_3$ nanoparticles,* Journal of Sol-Gel Science and Technology, (2024); https://doi.org/10.1007/s10971-024-06361-5.

М. Мокляк[1], Л. Кайкан[2], Ю. Мазуренко[2], М. Мойсеєнко[3], М. Кузишин[3], І. Довбня[3], Н. Ільницький[3], С. Юр'єв[4], В. Мокляк[2,5]

Вплив заміщення неодимом на термомагнітну відповідь та колоїдну поведінку наночастинок фериту міді

[1]*Кафедра прикладної фізики та матеріалознавства, Карпатський національний університет імені Василя Стефаника, Івано-Франківськ, Україна, mariamoklyak@gmail.com ;*
[2]*Лабораторія фізики магнітних плівок, Інститут металофізики імені Г.В. Курдюмова НАН України, Київ, Україна; alekstraza0@gmail.com, mvvmcv@gmail.com ;*
[3]*Кафедра медичної інформатики, медичної та біологічної фізики, Івано-Франківський національний медичний університет, Івано-Франківськ, Україна, mmoiseyenko@ifnmu.edu.ua, mkuzyshyn@ifnmu.edu.ua, Ilnytskyi_Na@ifnmu.edu.ua;*
[4]*Національний університет "Львівська політехніка", Львів, Україна, s.o.yuryev@gmail.com ;*
[5]*Кафедра фізико-математичних наук, Івано-Франківський національний технічний університет нафти і газу, Івано-Франківськ, Україна, volodymyr.mokliak@nung.edu.ua*

У даній роботі наночастинки $Cu_{1-x}Nd_xFe_2O_4$ (x = 0,00–0,11) були синтезовані методом золь-гель автогоріння та досліджені для оцінки впливу заміщення неодимом на їх структурні, магнітні та нагрівальні характеристики для застосування в магнітній гіпертермії. Рентгенівська дифракція підтвердила утворення шпінельних структур у всіх складах. Магнітні вимірювання продемонстрували немонотонну зміну намагніченості насичення (Ms), яка досягала максимального значення 62,11 emu/g при x = 0,05. Коерцитивна сила (Hc) коливалася в межах 236–273 E, що свідчить про вплив Nd^{3+}-заміщення на магнітну анізотропію системи. Відповідні часи релаксації за Нелем (τ_N) знаходилися в діапазоні приблизно 5–22 нс, що свідчить про ефективне магнітне нагрівання для окремих складів.

Вимірювання дзета-потенціалу засвідчили покращену колоїдну стабільність за умов помірного заміщення Nd, при якому значення перевищували +30 мВ для x = 0,03–0,07, що вказує на сприятливу дисперсність частинок для біомедичних застосувань. Ефективність магнітної гіпертермії досліджувалась у змінному магнітному полі (23,8 кА/м, 357 кГц) з використанням моделей Бокса–Люкаса та Ньютона. Найвищі значення питомого коефіцієнта поглинання (SAR) були зафіксовані для зразків з x = 0,03, 0,05 та 0,11. Отримані результати підкреслюють важливість ретельного підбору рівня заміщення рідкісноземельними іонами для керування поверхневим зарядом, магнітною анізотропією та механізмами релаксації.

Ключові слова: мідний ферит, неодимове заміщення, магнітні наночастинки, магнітна гіпертермія, енергоефективна терапія, метод Бокса-Лукаса, підхід охолодження Ньютона.